

# A simulation study of the impact of fracture networks on the co-production of geothermal energy and lithium

Shin Irgens Banshoya\*<sup>†</sup> Inga Berre<sup>†</sup> Eirik Keilegavlen<sup>†</sup>

## Abstract

Co-production of geothermal energy and lithium is an emerging opportunity with the potential to enhance the economic potential of geothermal operations. The economic reward of extracting lithium from geothermal brine is determined by how the lithium concentration evolves during brine production. In the initial stage, production will target lithium contained in the brine resident close to the production well. While lithium recharge, in the form of rock dissolution and inflow from other parts of the reservoir, is possible, the efficiency of such recharge depends on the geology of the reservoir. In this work, we study how structural heterogeneities in the form of fractures impact the flow of lithium-carrying brine. Using a numerical simulation tool that gives high resolution of flow and transport in fractures and the host rock, we study how the presence of fractures influences energy and lithium production. Our simulations show that, due to heat conduction and the lack of mineral recharge from the rock, differences in fracture network geometries have a much larger impact on lithium production than energy production. The simulations thus confirm that in addition to the geochemical characterisation of lithium in geothermal brines, understanding fracture characterisation and its impact on production is highly important for lithium production.

## 1 Introduction

The need for lithium is growing exponentially, driven by the need for rechargeable lithium batteries. As global demand for lithium is expected to increase by a factor of 40 from 2020 to 2040 in the IEA Sustainable Development Scenario (IEA, 2021), securing a reliable and diversified supply of lithium has become a top priority for many nations.

The substantial presence of lithium in geothermal brines presents an opportunity for the co-production of geothermal energy and lithium. For example, in both the US and Europe, several geothermal regions have lithium-rich brines, creating the potential for a domestic lithium supply chain (Sanjuan et al, 2022; Stringfellow and Dobson, 2020).

---

\*Corresponding author, shin.banshoya@uib.no

<sup>†</sup>Center for modeling of Coupled Subsurface Dynamics, Department of Mathematics, University of Bergen, Allegaten 41, Bergen, 5020, Norway

Operating geothermal systems typically involve a combination of injection and production wells. Re-injection is essential for disposing of the cooled produced fluids and maintaining the reservoir pressure. However, in many cases, this process leads to the breakthrough of re-injected fluids (Gringarten, 1978; Stefansson, 1997; Li et al, 2016). As a result, progressively higher concentrations of re-injected fluids are produced. Over time, this leads to lower temperatures of the produced fluid. In geothermal-lithium co-production, lithium production rates are expected to decline over time due to the chemical breakthrough of lithium-depleted re-injection fluid. While the rate at which lithium leaches from the rock may be too low to significantly increase the lithium concentration in the re-injected fluid (Jungmann et al, 2024), conductive heat transfer between rock and fluid and between warmer and colder regions will contribute to the heating of the injected fluid. This leads to an earlier chemical breakthrough compared to thermal breakthrough (Goldberg et al, 2023).

The timing of chemical and thermal breakthroughs, along with subsequent declines in lithium and heat production, is influenced by the flow field in the reservoir (Dobson et al, 2023; Goldberg et al, 2023). The flow field is primarily determined by the pressure gradients induced through injection and production combined with the permeability of the formation. Structural heterogeneity in permeability, resulting, for example, from features such as networks of faults and fractures, plays a crucial role in determining the flow in the system (Moreno and Tsang (1994); Egert et al (2020)). For example, if fractures form high-permeable pathways between the injection and production well, the injection fluid will reach the production well early, and the subsequent ratio of injected fluid that is produced will be large (flow-short circuiting) (Liu et al, 2020; Fadel et al, 2022). In contrast, if fractures provide high-permeable pathways connecting the wells to other parts of the reservoir, this will hamper the breakthrough of injected fluid in the production well, and even after injected fluid has reached the production well, the ratio of injected fluid that is produced will be low.

The large effect fractures and faults have on fluid flow also affects lithium and energy production, but the relative effect on lithium and energy production is not the same (Goldberg et al, 2023). At the pore scale, heat is transferred from the solid rock to the colder injected fluids, while at the continuum scale, conduction transfers heat from high to low-temperature regions. The large aspect ratio of fractures implies that conductive heat transfer from the surrounding porous formation will contribute significantly to heating the injected fluid. These heat transfer mechanisms dampen the effect of the convective heat transfer dictated by the flow field and, hence, the effect the fracture network geometry has on the thermal breakthrough. In contrast, lithium production is more dictated by the flow field as the concentration transport is mainly driven by advection (Goldberg et al, 2023). It will, therefore, to a higher degree, be influenced by fracture network geometry. In summary, models that include the effect of faults and fractures are needed to optimise re-injection schemes for the combined production of geothermal energy and lithium.

In this study, we explore the influence of fractures on chemical and thermal breakthroughs in geothermal lithium co-production using a mathematical model and corresponding numerical approach that simulates heat transfer and solute transport in fractured porous media. Our goal is to investigate the hypothesis that differences in fracture network geometry have a larger impact on lithium production than energy production.



The model integrates fluid flow, convective and conductive heat transfer, and solute transport of lithium-depleted re-injection fluid within a fractured reservoir. Although water-rock interactions can potentially leach lithium from minerals into the reservoir fluid (Drüppel et al, 2020; Regenspurg et al, 2016), experimental data necessary for accurately quantifying this effect in simulation models are lacking. Therefore, we adopt a conservative approach and assume that the leaching of lithium from rock minerals into the lithium-depleted re-injection fluid is negligible (Dobson et al, 2023). The model is based on an explicit representation of fractures, which are treated as objects of one dimension lower than the surrounding medium (Martin et al, 2005). This mixed-dimensional model accurately represents the processes in the fractures and their interaction with matrix processes (Berre et al, 2021).

The article is structured as follows. We present the mathematical model and numerical approach in Sec. 2. We present the simulation results in Sec. 3. Finally, we give conclusions in Sec. 4.

## 2 Mathematical model and numerical approach

We consider a fractured porous media where, following (Martin et al, 2005), the fractures are treated as two-dimensional surfaces in three-dimensional domains and one-dimensional lines in two-dimensional domains. This section presents the governing model equations for flow and transport in the matrix and fractures, respectively, and the equations defining the coupling between the matrix and fractures. A short review of the numerical approach is given at the end.

### 2.1 Matrix equations

We consider incompressible single-phase flow, modelled by Darcy’s law and the mass conservation equation

$$\mathbf{v} = -\frac{\mathcal{K}}{\eta}\nabla p, \quad (1)$$

$$\nabla \cdot \mathbf{v} = f_p, \quad (2)$$

where  $\mathbf{v}$ ,  $\mathcal{K}$ ,  $\eta$  and  $p$  are the Darcy flux, the permeability, the dynamic viscosity and the pressure, respectively. Lastly,  $f_p$  is the volumetric flow rate per unit bulk volume that accounts for the well injection and production. With  $\mathbf{q}$  denoting a constant flow rate, it is defined as

$$f_p = \begin{cases} \mathbf{q}, & \text{injection points,} \\ -\mathbf{q}, & \text{production points,} \\ 0. & \text{elsewhere.} \end{cases}$$

Neglecting dispersion, the non-reactive transport equation for the lithium concentration reads

$$\partial(\phi c) + \nabla \cdot (c\mathbf{v}) = f_c, \quad (3)$$

where  $\phi$  is the porosity,  $c$  is the molar lithium concentration and

$$f_c = \begin{cases} c_{\text{in}}\mathbf{q}, & \text{injection point,} \\ -c\mathbf{q}, & \text{production point,} \\ 0, & \text{elsewhere,} \end{cases}$$

the accounts for the injection and production of the lithium concentration, with  $c_{\text{in}}$  being the injected concentration.

The temperature,  $T$ , evolves due to convective heat flux and Fourier's law in an energy conservation equation. We further assume local thermal equilibrium and, hence, write the energy conservation equation as

$$\partial_t((\rho b)_m T) + \nabla \cdot ((\rho b)_f T \mathbf{v} - \kappa_m \nabla T) = f_T. \quad (4)$$

Here,  $(\rho b)_m = \phi(\rho b)_f + (1 - \phi)(\rho b)_s$  and  $\kappa_m = \phi\kappa_f + (1 - \phi)\kappa_s$  are the effective heat capacity and thermal conductivity, respectively, with the subscripts  $f$  and  $s$  referring to the fluid and solid rock. The density, the specific heat capacity and the thermal conductivity are denoted  $\rho$ ,  $b$  and  $\kappa$ , respectively, where the subscript indicates if they are a fluid or a solid rock parameter. These parameters are taken to be constant. Finally,  $f_T$  represents the injection and production rate of the temperature,

$$f_T = \begin{cases} (\rho b)_f T_{\text{in}} \mathbf{q}, & \text{injection point,} \\ -(\rho b)_f T \mathbf{q}, & \text{production point,} \\ 0, & \text{elsewhere,} \end{cases}$$

where  $T_{\text{in}}$  is the injected temperature.

## 2.2 Fracture equations

This section describes the partial differential equations in fractures and fracture intersections. We use the modelling strategy of treating fractures as lower-dimensional objects embedded in the porous matrix, joint with interface conditions for the matrix-fracture interaction. Since this modelling approach has been presented in detail several times before (e.g. Berre et al, 2021; Gläser et al, 2022; Keilegavlen et al, 2021; Frih et al, 2012; Budiša and Hu, 2021; Hyman et al, 2022, and references therein), we simplify the presentation given here by considering only a single fracture in a porous medium and refer to the mentioned references for the more general case with several fractures, as well as how this modelling strategy includes fracture intersections.

Following the domain decomposition of Martin et al (2005) and Boon et al (2018), the  $d$ -dimensional fractured porous medium  $\Omega$ ,  $d = 2, 3$ , is decomposed into two subdomains. The first is  $\Omega_h$ , the  $d$ -dimensional porous matrix subdomain, and the second is  $\Omega_l$ , the  $(d - 1)$ -dimensional fracture subdomain. The two subdomains are connected by two interfaces,  $\Gamma_+$  and  $\Gamma_-$ , and two internal matrix boundaries,  $\partial_+ \Omega_h$  and  $\partial_- \Omega_h$ . Fig. 1 shows the connection between the matrix and the fracture. In the following, a variable with the subscript  $h$  or  $l$  belongs to  $\Omega_h$  or  $\Omega_l$ , respectively. Similarly, a variable with the subscript  $+$  or  $-$  belongs to  $\Gamma_+$  or  $\Gamma_-$ .

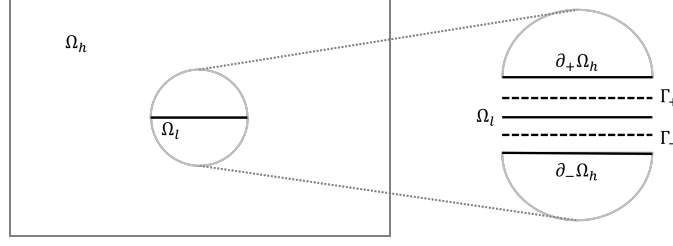


Figure 1: Illustration of mixed-dimensional representation of a fractured porous medium with matrix  $\Omega_h$  and one fracture  $\Omega_l$ . The internal boundaries of  $\Omega_h$ ,  $\partial_+\Omega_h$  and  $\partial_-\Omega_h$ , and the interfaces,  $\Gamma_+$  and  $\Gamma_-$ , between  $\Omega_h$  and  $\Omega_l$  are shown to the right.

The flow equations in the fracture read

$$\mathbf{v}_l = -\epsilon_l \frac{\mathcal{K}_l}{\eta_l} \nabla p_l, \quad (5)$$

$$\nabla \cdot \mathbf{v}_l = \epsilon_l f_p + (v_+ + v_-)|_{\Omega_l}. \quad (6)$$

In these equations, the scaling by the aperture,  $\epsilon_l$ , accounts for the dimension reduction. The aperture also governs the fracture permeability via the cubic law,

$$\mathcal{K}_l = \epsilon_l^2/12.$$

Furthermore, the nabla operator and the fracture permeability operate in the tangential direction of the fracture. Lastly,  $v_+$  and  $v_-$  on the right-hand side in Eq. (6) represent interface fluxes that account for the fracture flow coupling to the matrix flow. They are modelled by the Darcy-type equation (Martin et al, 2005)

$$v_j = -\frac{2\mathcal{K}_l|_{\Gamma_j}}{(\eta\epsilon)_l|_{\Gamma_j}} (p_l|_{\Gamma_j} - p_h|_{\Gamma_j}), \quad (7)$$

where the subscript  $j$  refers to either the  $+$  or  $-$  side of the fracture.

The matrix flow Eqs. (1)-(2) are coupled to the fracture flow equations through an internal Neumann condition

$$(\boldsymbol{\nu}_h \cdot \mathbf{v}_h)|_{\partial_j \Omega_h} = v_j|_{\partial_j \Omega_h}. \quad (8)$$

The transport equation for the concentration in the fracture is

$$\partial(\epsilon_l \phi_l c_l) + \nabla \cdot (c_l \mathbf{v}_l) = \epsilon_l f_c + (\zeta_+ + \zeta_-)|_{\Omega_l}. \quad (9)$$

The advective interface flux,  $\zeta_j$ , is calculated as

$$\zeta_j = \begin{cases} v_j c_h|_{\Gamma_j}, & \text{if } v_j \geq 0, \\ v_j c_l|_{\Gamma_j}, & \text{if } v_j < 0, \end{cases} \quad (10)$$

and appears in the following Neumann condition for  $\Omega_h$

$$(\boldsymbol{\nu}_h \cdot c_h \nabla_h)|_{\partial_j \Omega_h} = \zeta_j|_{\partial_j \Omega_h}. \quad (11)$$

Finally, the energy conservation equation in the fracture is

$$\begin{aligned} \partial_t(\epsilon_l(\rho b)_{\mathbf{m},l}T) + \nabla \cdot ((\rho b)_{\mathbf{f},l}T_l \mathbf{v}_l - \epsilon_l \kappa_{\mathbf{m},l} \nabla T_l) = \\ \epsilon_l f_T + \{(w_+ + q_+) + (w_- + q_-)\}|_{\Omega_l}, \end{aligned} \quad (12)$$

with the internal boundary conditions

$$(\mathbf{v}_h \cdot (\rho b)_{\mathbf{f},h} T_h \mathbf{v}_h)|_{\partial_j \Omega_h} = w_j|_{\partial_j \Omega_h}, \quad (13)$$

$$(\mathbf{v}_h \cdot -\kappa_{\mathbf{m},h} \nabla T_h)|_{\partial_j \Omega_h} = q_j|_{\partial_j \Omega_h}. \quad (14)$$

The interface convective and conductive fluxes,  $w_j$  and  $q_j$ , are calculated as

$$w_j = \begin{cases} \mathbf{v}_j \cdot ((\rho b)_{\mathbf{f},h} T_h)|_{\Gamma_j}, & \text{if } \mathbf{v}_j \geq 0, \\ \mathbf{v}_j \cdot ((\rho b)_{\mathbf{f},l} T_l)|_{\Gamma_j}, & \text{if } \mathbf{v}_j < 0, \end{cases} \quad (15)$$

$$q_j = -\frac{2\kappa_{\mathbf{f},l}|_{\Gamma_j}}{\epsilon_l|_{\Omega_l}} (T_l|_{\Gamma_j} - T_h|_{\Gamma_j}). \quad (16)$$

### 2.3 Numerical approach

Since the flow field will be constant based on the choice of boundary conditions and source term, the flow Eqs. (1)-(2), (5)-(8) are solved once at the beginning of the simulation to obtain the flow field used to solve for temperature and lithium concentration in time. Then, in the time loop, the remaining equations (Eqs. (3)-(4), (9)-(16)) are solved.

The equations are discretised and solved using functionality from the open-source software PorePy (Keilegavlen et al, 2021). The simulation meshes in PorePy are constructed to conform to fractures in accordance with the modelling principles employed in Section 2.2, with the actual mesh generation handled by a Gmsh backend (Geuzaine and Remacle, 2009). For the spatial discretisation, we use the cell-centred finite volume methods implemented in PorePy. Specifically, a two-point flux approximation is used for the elliptic terms, and the standard first-order upwind scheme is used for the advective terms. The interface fluxes are calculated using the subdomain variables evaluated at the internal boundaries. For temporal discretisation, we employ the implicit Euler scheme. The full discretisation of the unsteady PDEs leads to a system of linear equations, which is solved by the solver PyPardiso (Haas, 2023).

## 3 Simulations of evolution of lithium concentration and temperature

This section presents simulations that investigate the effect of fractures on lithium concentration and temperature in the reservoir during production, as well as their effect on the produced lithium concentration and temperature. We start by considering stochastically generated fracture networks for different fracture densities in a two-dimensional domain. We then consider a three-dimensional test case that illustrates the effect of fracture network connectivity on lithium concentration and temperature for a more realistic setup in terms of fracture network geometry. The fluid and rock parameters are constant for all the simulations and are listed in Table 1.

Table 1: Constant simulation parameters for the simulations in Sections 3.1 and 3.2.

Parameter	Value
Dynamic viscosity ( $\eta$ )	$10^{-3}$ Pa s
Matrix porosity	0.2 [-]
Fracture porosity	1.0 [-]
Matrix permeability ( $\mathcal{K}$ )	$1.0 \cdot 10^{-13}$ m <sup>2</sup>
Fracture aperture ( $\epsilon$ )	$5 \cdot 10^{-3}$ m
Fluid density ( $\rho_f$ )	1000 kg/m <sup>3</sup>
Solid density ( $\rho_s$ )	2750 kg/m <sup>3</sup>
Fluid specific heat capacity ( $b_f$ )	4200 J/(kg K)
Solid specific heat capacity ( $b_s$ )	790 J/(kg K)
Fluid thermal conductivity ( $\kappa_f$ )	0.6 W/(m K)
Solid thermal conductivity ( $\kappa_s$ )	3.0 W/(m K)

### 3.1 Stochastically generated fracture networks in two dimensions

To study the impact of fractures on lithium and energy production, we consider stochastically generated fracture networks in a two-dimensional domain with different fracture densities. The two-dimensional domain can be considered as a horizontal slice of unit thickness taken out of a 3d formation with vertical fractures.

#### 3.1.1 Setup

The computational domain is  $\Omega = [0, 3]$  km  $\times$   $[0, 2]$  km, with an injection well at (1, 1) km and a production well at (2, 1) km. We assume that the fracture centres,  $(x_c, y_c)$ , follow a uniform distribution

$$\begin{aligned} x_c &\sim U([0, 3000]), \\ y_c &\sim U([0, 2000]). \end{aligned}$$

Furthermore, the fracture length follows a lognormal distribution, with a mean of 500 m and a standard deviation of 200 m. The orientation is generated from a uniform distribution,  $U[-\pi/2, \pi/2]$ .

We use the number of fractures to measure the fracture network density and consider three cases with 8, 30 and 82 fractures in the domain, respectively. Fig. 2 shows an example of a generated fracture network for each density. The lowest fracture density is considered to represent a case where the fractures have a low probability of forming high-permeable connected pathways between the wells. In the highest considered fracture density, the fracture network will, with a very high probability, provide long, high-permeable pathways for the fluid flow and thus completely dominate the transport of energy and lithium.

Before production, the reservoir is assumed to have an initial temperature of 160°C and an initial lithium concentration of 170 mg/L. For pressure, we set the constant value of 30 MPa at the boundary of the domain, which will allow for fluid flow in and out of the simulation domain due to pressure differences

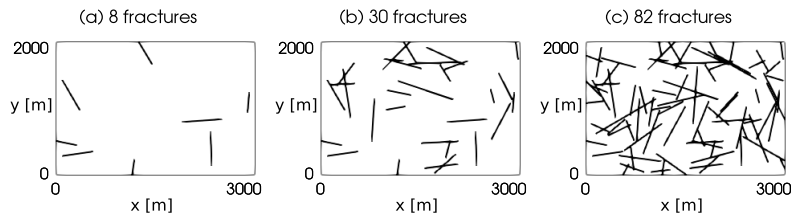


Figure 2: Example of stochastically generated fracture networks with (a) 8, (b) 30 and (c) 82 fractures.

induced by the injection and production. The injection temperature is  $70^{\circ}\text{C}$ , and the lithium concentration of the injected fluid is  $0\text{ mg/L}$ . The injection and production rate is  $q = 0.4\text{ L/s}$ , corresponding to a rate of  $40\text{ L/s}$  for a formation with a thickness of  $100\text{ m}$ . Lastly, the time step is set constant to  $4.73 \cdot 10^7\text{ s}$  ( $1.5\text{ years}$ ).

### 3.1.2 Results

To exploit the effect of fracture network geometry on the spatial evolution of lithium concentration and temperature in the reservoir, we first discuss the results for two fracture network realisations with 82 fractures, R1 and R2. The network R1 is meshed with 13239 matrix and 1434 fracture cells, and the network R2 is meshed with 14881 matrix and 1602 fracture cells.

Figs. 3 and 4 show the lithium concentration and temperature in the reservoir after 4.5 years, 25.5 years and 60 years for R1 and R2, respectively. As can be seen from the figures, the lithium concentration and temperature evolve in the reservoir fundamentally different for the two different fracture networks: For R1, the fracture network provides preferential pathways for flow and transport towards the left boundary of the domain. In contrast, for R2, the fracture network provides a preferential pathway between the injection and production wells, leading to flow short-circuiting between the wells. The result is very different spatial profiles for lithium concentration and temperature for the two fracture networks. Though the figures also show some numerical diffusion, this does not significantly impact the production curves.

The difference in production between R1 and R2 is striking, as can be seen in Fig. 5, where the lithium concentration and temperature in the production well are shown as a function of time. For R2, the breakthrough of lithium-depleted injected fluid in the production well happens early. After approximately 10 years, the decline in produced concentration is already almost 80% of the maximum possible decline. In comparison, for the network R1, the decline in produced concentration is nearly 15% after about 10 years.

Compared to the decline in concentration of produced lithium, the decline in production temperature is slower. This is expected, as heat is transferred from the solid rock to the fluids locally in the porous matrix, and since, in addition to convective heat transfer, conduction transfers heat from high to low-temperature regions. After approximately 10 years, the decline in produced temperature is around 2% of the maximum possible decline for R1, while it is nearly 25% for R2.

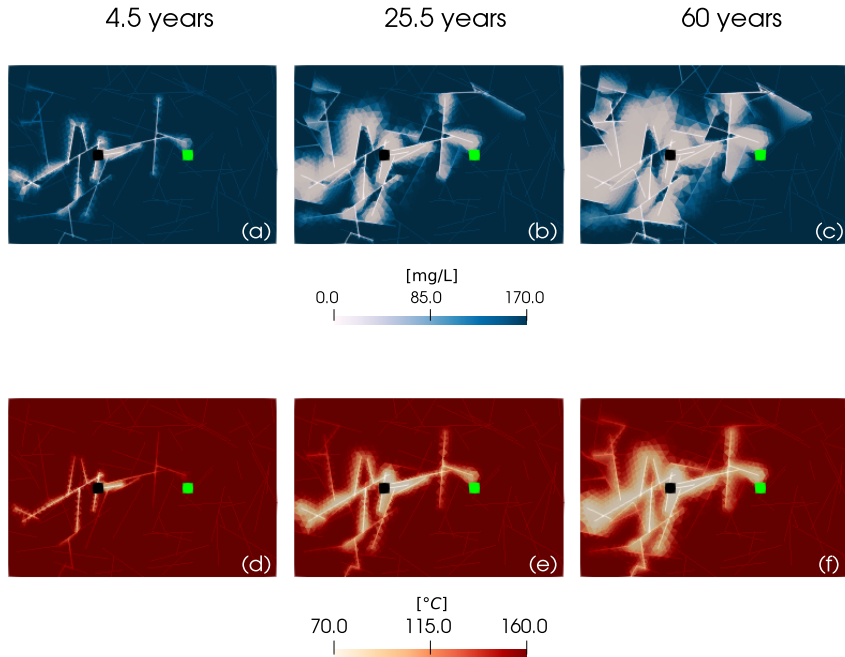


Figure 3: The spatial solution in the network R1 at different times. Lithium concentration after (a) 4.5, (b) 25.5 and (c) 60 years, and temperature after (d) 4.5, (e) 25.5 years and (f) 60 years. The black and green squares represent the injection and production wells, respectively.

From Fig. 5, when comparing the results obtained with R1 and R2, it is clear that the relative difference over time is larger in lithium production than in energy production. As this effect is consistent over time, the flow short-circuiting between the wells caused by the geometry of R2 will have a larger negative impact on the cumulative lithium production than energy production (relative difference of area under the graphs in Fig. 5).

We next discuss the outcome of running 10,000 realisations for each fracture density to further study the effects of fracture network geometries.

Fig. 6 shows the temporal evolution of concentration and temperature in the production cell, joint with the 10th, 50th and 90th percentiles (P10, P50 and P90). For all fracture densities and P10, P50 and P90 curves, the front of low lithium concentration reaches the production well faster than the front of low temperature, as the latter experiences the combined effect of diffusion and the need to cool down the rock. Notably, for the lithium concentration, the P90 curves show an almost immediate breakthrough for both the intermediate (30) and high (82) fracture densities; in the latter case, the P50 curve also indicates a rapid breakthrough. By comparison, a rapid breakthrough is only achieved for the P90 curve in the high-density regime for the cold temperature front.

We also see that increasing fracture density increases the likelihood (represented by the P10 curve) of a delayed breakthrough. This can be attributed to the fracture network leading the injected fluid away from the production well. Although the limited domain size has some impact on the simulations, we be-

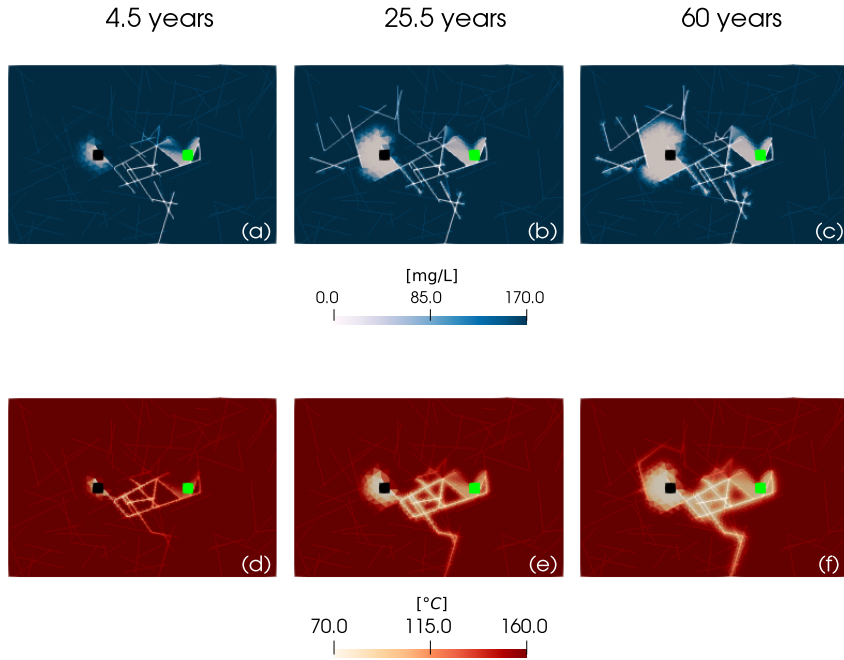


Figure 4: The spatial solution in the network R2 at different times. Lithium concentration after (a) 4.5, (b) 25.5 and (c) 60 years, and temperature after (d) 4.5, (e) 25.5 years and (f) 60 years. The black and green squares represent the injection and production wells, respectively.

lieve this effect would also have been present for larger domains. Nevertheless, the P10 curves also show that the lithium concentration in the production well decreases faster than the temperature.

Fig. 7 shows the frequency of the extracted lithium concentration,  $W_c$ , and temperature,  $W_T$ , accumulated over the production period, together with the associated P10, P50 and P90. The cumulative quantities are calculated as

$$W_c = \int_0^{60} c q dt, \quad W_T = \int_0^{60} T \rho_f b_f q dt$$

The trapezoidal method is used to estimate the integrals. By comparing lithium and energy production, it can immediately be seen that the relative span in the cumulative production is larger for lithium concentration than for temperature. Comparing the P50 curves for the different fracture densities, we can see no large difference in total production in the period. However, the variation in the cumulative production is larger with an increasing number of fractures. Considering the P10 and P90 curves, over the 60-year production period, the difference between P10 and P90 in cumulative production is larger for lithium than for energy for all three fracture densities but increases with larger densities. As noted earlier, a high fracture density impacts production both positively and negatively, as the fracture networks either provide short pathways between the injection and production wells or spread the transported quantities more widely in the domain.



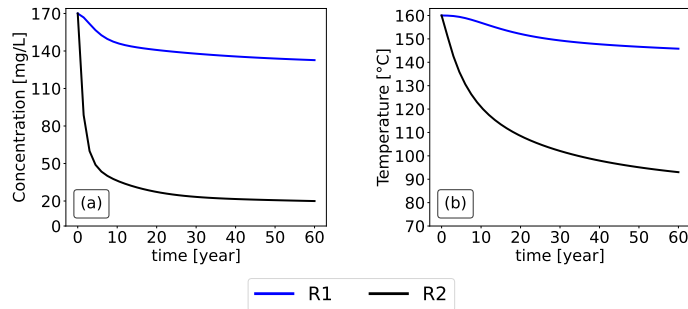


Figure 5: Lithium concentration (a) and temperature (b) in the production well as a function of time for R1 and R2.

In Appendix A, we demonstrate the convergence of the Monte Carlo simulations.

### 3.2 Fracture networks in three-dimensions

In this section, we consider a three-dimensional fractured domain to exploit the characteristics identified for the two-dimensional simulations in a more realistic fracture network geometry. The fracture network geometry is inspired by information from the Soultz-sous Forêts geothermal site (Sausse et al, 2010). The network (N1) consists of 39 fractures; a subset of these is illustrated in Fig. 8, which also shows the injection and production well, respectively. The simulation domain is  $\Omega = [-4, 2] \text{ km} \times [-3, 3] \text{ km} \times [0, 8] \text{ km}$ .

For the fracture network N1, the fractures do not form a connected network between the wells; see Fig. 9a. To investigate the effect of connectivity, we consider a second fracture network, N2, where we have introduced an additional fracture to the network N1 that links the disconnected parts of the N1 fracture network; see Fig. 9(b).

For the simulation with the fracture network N1, the matrix is meshed with 87072 cells, and the fractures are meshed with a total of 11032 cells. For the simulation with N2, the matrix is meshed with 86208 cells, and the fractures are meshed with a total of 11213 cells. The flow rate in the injection and production well is set to  $q = 30 \text{ L/s}$ , and the pressure is 30 MPa at all global boundaries. For the lithium concentration and temperature, the initial conditions, injection and boundary values are the same as in Section 3.1. The time step is set constant to  $3.15 \cdot 10^7 \text{ s}$  (1 year).

Fig. 10 shows simulation results in the fracture networks N1 and N2 after 1 year and 60 years. As seen, the lithium concentration enters the computational domain from the injection well and propagates in the surrounding fracture network. For the simulation with the fracture network N1, where the fractures do not provide a direct connection between the injection and production cells, Figs. 10a-b show that the front of low concentration does not reach the production well. In contrast, for the simulation with the fracture network N2, Figs. 10c-d shows that the extra fracture creates a highly conductive pathway directly from the injection to the production well, which results in the breakthrough of the lithium-depleted fluid in the production well.

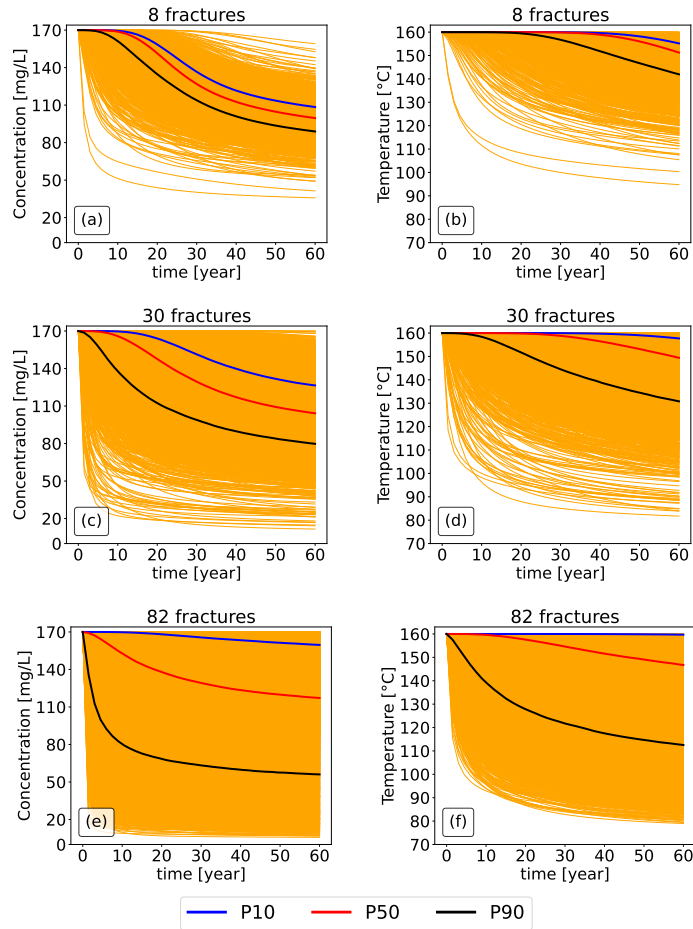


Figure 6: The 10,000 realisations (in orange) of the evolution of the lithium concentration (left column) and temperature (right column) in the production well, for fracture networks with 8 ((a), (b)), 30 ((c), (d)) and 82 ((e), (f)) fractures, joint with P10, P50 and P90 curves.

For the temperature, its front does not reach the production well for either of the fracture networks. For N2, Figs. 10e-f shows that the front of temperature does not migrate past the fracture where the injection well is located. This is caused by the heat conduction into the injection fracture and the corresponding cooling of the rock matrix near the injection well.

Fig 11a displays the evolution of the concentration at the production well. In accordance with the spatial distribution of the lithium concentration, no reduction in the extracted lithium concentration is observed with N1. In contrast, for N2, the extracted lithium concentration is reduced from an early simulation time. For the energy production, no reduction in produced temperature is observed for either of the fracture networks, as observed in Fig. 11b. The example thus further underlines the importance of fracture connectivity and the different impact this has on energy and lithium production.

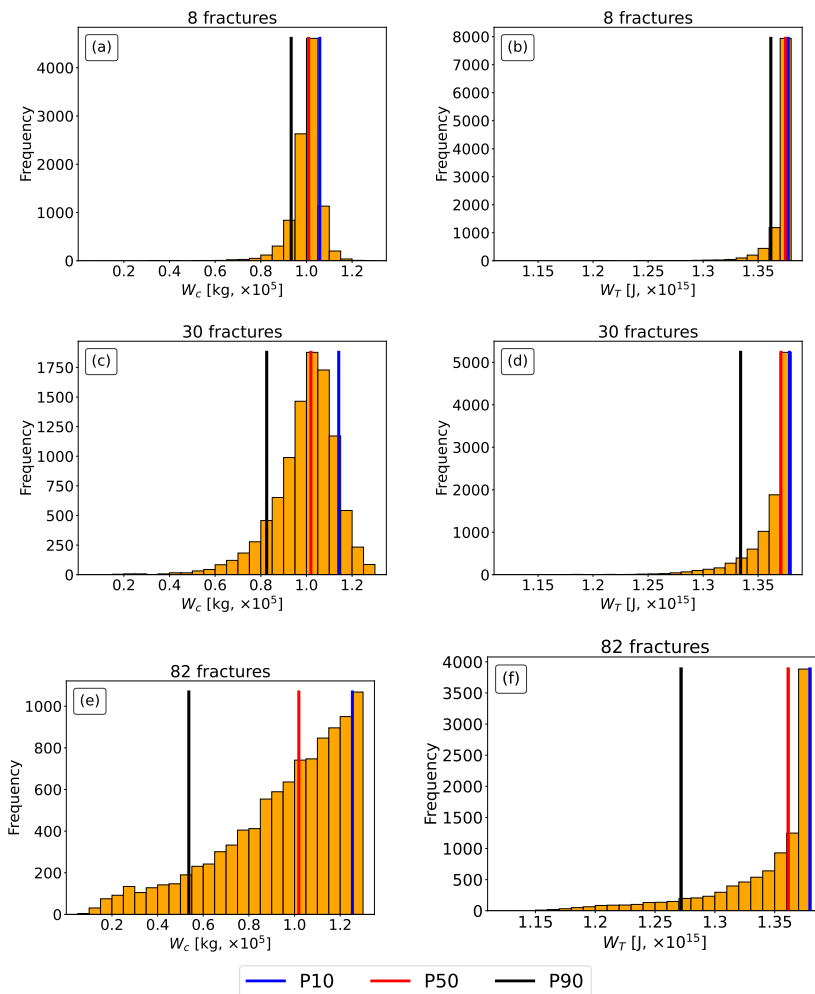


Figure 7: Frequency histograms of the cumulative lithium ((a), (c), (e)) and energy ((b), (d), (f)) production for the different fracture densities.

## 4 Conclusion

In this paper, we have numerically investigated the influence of fractures on the co-production of lithium and energy for the case of a geothermal doublet system where produced water is re-injected into the reservoir.

We have studied the difference in lithium concentration and temperature production from two-dimensional simulations with stochastically generated fracture geometries for different fracture densities. The simulations show that the impact of fractures is different for energy and lithium production, and the behaviour expected for energy production cannot readily be transferred to lithium production. Breakthrough of re-injected water causes a decline in both lithium concentration and temperature of the produced fluid. As expected, the decline in the lithium concentration always starts earlier than the decline in the temperature.

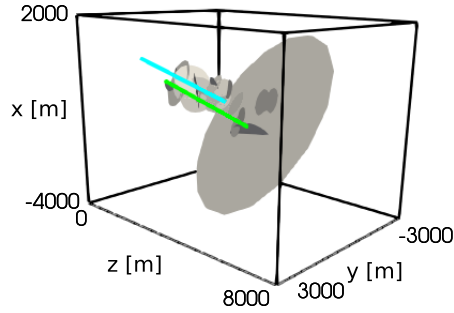


Figure 8: The fracture network N1 in the matrix. The black lines represent the global matrix boundaries, and the blue and green lines represent the injection and production well.

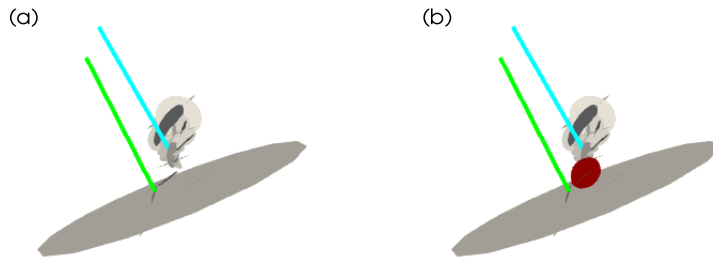


Figure 9: The fracture network N1 (a), where the fractures do not form a connected network between the injection and production well, and network N2 (b), where an additional fracture (illustrated in red) is added to the network N1.

Over time, the relative reduction, compared to the case where the re-injected water does not reach the production well, will always be larger for cumulative lithium production than for energy production. In terms of cumulative production, lithium production shows larger variation with different fracture geometries than energy production. Hence, our results corroborate the hypothesis that differences in fracture network geometry have a larger impact on lithium production than energy production.

In the geothermal community, the importance of fractures and fracture network connectivity on energy production from a doublet configuration with injection and production well is well known and has been studied extensively. This paper shows that the impact of fractures and variety in fracture network geometry is even more important considering lithium production. Hence, modelling studies that appropriately account for the effect of fractures are crucial in estimating lithium production.

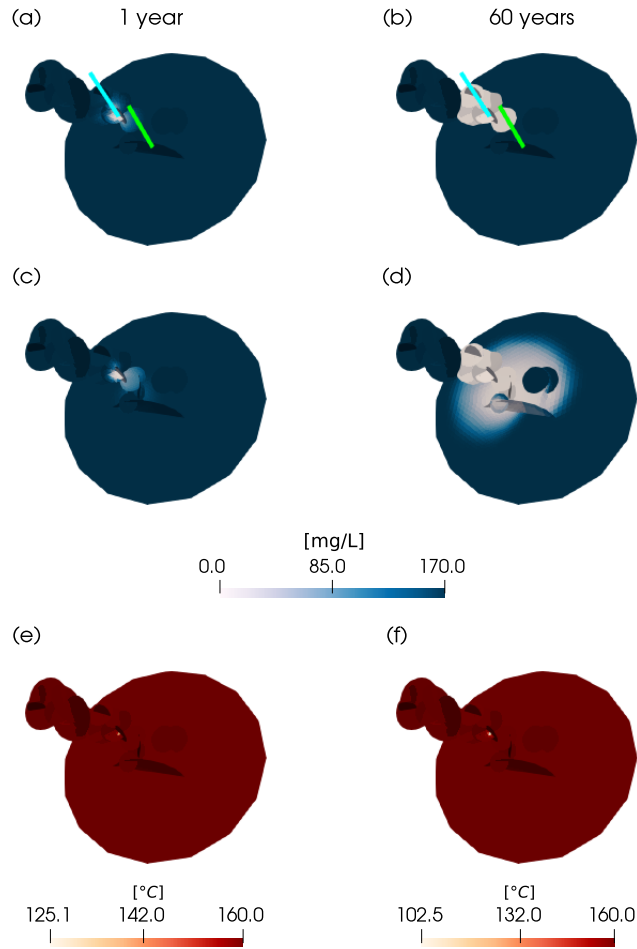


Figure 10: The simulation results after 1 year (left column) and 60 years (right column). (a) and (b) exhibit the lithium concentration in N1. (c) and (d) exhibit the lithium concentration in N2. (e) and (f) exhibit the temperature in N2.

## Acknowledgements

This work was financed by the Norwegian Research Council grant number 308733. The second author also acknowledges funding from the VISTA program, The Norwegian Academy of Science and Letters and Equinor.

## Appendix A

In this appendix, we demonstrate the convergence of the Monte Carlo simulations in Sec. 3.1 To assess the convergence, we have used an approach similar to that used by Wang et al (2023) and Cremon et al (2020).

Fig. 12 shows the sample mean, P10, P50 and P90 of the extracted concentration and temperature after 60 years as a function of the realisations for the

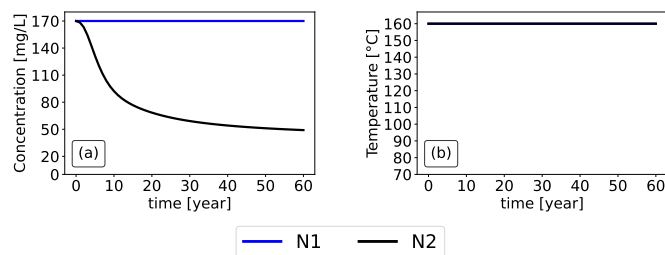


Figure 11: The lithium concentration (a) and temperature (b) evolution at the production cell for the simulation with the fracture networks N1 and N2.

density with 30 fractures. The curves in Fig. 12a are constructed as follows. We calculate the sample mean of the dataset that contains the  $n$  first realised concentrations after 60 years,  $n = 1, 2, 3, \dots, 10,000$ . The sample mean of the concentration is recalculated with the increasing number of realised concentrations. When this step is done, we resample the realised concentrations and calculate the sample mean of the resampled concentrations in the same fashion. The reshuffling procedure is repeated 300 times, and Fig. 12a shows everything put together. Fig. 12b demonstrates the outcome of this procedure applied to the temperature. Figs 12c-h show the procedure applied on P10, P50 and P90. A clear convergence is observed for all the plotted quantities. We observed a similar convergence for the networks with 8 and 82 fractures.

## References

- Berre I, Boon WM, Flemisch B, et al (2021) Verification benchmarks for single-phase flow in three-dimensional fractured porous media. *Advances in Water Resources* 147:103759. <https://doi.org/10.1016/j.advwatres.2020.103759>
- Boon WM, Nordbotten JM, Yotov I (2018) Robust discretization of flow in fractured porous media. *SIAM Journal on Numerical Analysis* 56(4):2203–2233. <https://doi.org/10.1137/17M1139102>
- Budiša A, Hu X (2021) Block preconditioners for mixed-dimensional discretization of flow in fractured porous media. *Computational Geosciences* 25:671–686. <https://doi.org/10.1007/s10596-020-09984-z>
- Cremon MA, Christie MA, Gerritsen MG (2020) Monte carlo simulation for uncertainty quantification in reservoir simulation: A convergence study. *Journal of Petroleum Science and Engineering* 190:107094. <https://doi.org/10.1016/j.petrol.2020.107094>
- Dobson P, Araya N, Brounce M, et al (2023) Characterizing the geothermal lithium resource at the salton sea. Tech. rep., Lawrence Berkeley National Laboratory (LBNL), Berkeley, CA (United States)
- Drüppel K, Stober I, Grimmer JC, et al (2020) Experimental alteration of granitic rocks: Implications for the evolution of geothermal brines in the upper rhine graben, germany. *Geothermics* 88:101903

- Egert R, Korzani MG, Held S, et al (2020) Implications on large-scale flow of the fractured egs reservoir soultz inferred from hydraulic data and tracer experiments. *Geothermics* 84:101749
- Fadel M, Reinecker J, Bruss D, et al (2022) Causes of a premature thermal breakthrough of a hydrothermal project in germany. *Geothermics* 105:102523
- Frih N, Martin V, Roberts JE, et al (2012) Modeling fractures as interfaces with nonmatching grids. *Computational Geosciences* 16:1043–1060. <https://doi.org/10.1007/s10596-012-9302-6>
- Geuzaine C, Remacle JF (2009) Gmsh: A 3-d finite element mesh generator with built-in pre-and post-processing facilities. *International journal for numerical methods in engineering* 79(11):1309–1331
- Gläser D, Schneider M, Flemisch B, et al (2022) Comparison of cell- and vertex-centered finite-volume schemes for flow in fractured porous media. *Journal of Computational Physics* 448:110715. <https://doi.org/10.1016/j.jcp.2021.110715>
- Goldberg V, Dashti A, Egert R, et al (2023) Challenges and opportunities for lithium extraction from geothermal systems in germany—part 3: the return of the extraction brine. *Energies* 16(16):5899
- Gringarten AC (1978) Reservoir lifetime and heat recovery factor in geothermal aquifers used for urban heating. *Pure and applied geophysics* 117:297–308
- Haas A (2023) Pypardiso. <https://github.com/haasad/PyPardisoProject>
- Hyman JD, Sweeney MR, Gable CW, et al (2022) Flow and transport in three-dimensional discrete fracture matrix models using mimetic finite difference on a conforming multi-dimensional mesh. *Journal of Computational Physics* 466:111396. <https://doi.org/10.1016/j.jcp.2022.111396>
- IEA (2021) The role of critical world energy outlook special report minerals in clean energy transitions, world energy outlook special report. Tech. rep., International Energy Agency
- Jungmann M, Walter BF, Eiche E, et al (2024) The source of lithium in connate fluids: Evidence from the geothermal reservoir at soultz-sous-forêts, upper rhine graben, france. available at ssrn: <https://ssrn.com/abstract=4873662> or <http://dx.doi.org>. Available at SSRN <https://doi.org/10.2139/ssrn.4873662>
- Keilegavlen E, Berge R, Fumagalli A, et al (2021) PorePy: An open-source software for simulation of multiphysics processes in fractured porous media. *Computational Geosciences* 25(1):243–265. <https://doi.org/10.1007/s10596-020-10002-5>
- Li T, Shiozawa S, McClure MW (2016) Thermal breakthrough calculations to optimize design of a multiple-stage enhanced geothermal system. *Geothermics* 64:455–465

- Liu H, Wang H, Lei H, et al (2020) Numerical modeling of thermal breakthrough induced by geothermal production in fractured granite. *Journal of Rock Mechanics and Geotechnical Engineering* 12(4):900–916
- Martin V, Jaffré J, Roberts JE (2005) Modeling fractures and barriers as interfaces for flow in porous media. *SIAM Journal on Scientific Computing* 26(5):1667–1691
- Moreno L, Tsang CF (1994) Flow channeling in strongly heterogeneous porous media: A numerical study. *Water Resources Research* 30(5):1421–1430
- Regenspurg S, Feldbusch E, Norden B, et al (2016) Fluid-rock interactions in a geothermal rotliegend/permo-carboniferous reservoir (north german basin). *Applied Geochemistry* 69:12–27
- Sanjuan B, Gourcerol B, Millot R, et al (2022) Lithium-rich geothermal brines in Europe: An up-date about geochemical characteristics and implications for potential Li resources. *Geothermics* 101:102385. <https://doi.org/10.1016/j.geothermics.2022.102385>
- Sausse J, Dezayes C, Dorbath L, et al (2010) 3d fracture zone network at soultz based on geological data, image logs, microseismic events and vsp results. *CR Geoscience* 342(2010):531–545. <https://doi.org/http://dx.doi.org/10.1016/j.crte.2010.01.011>
- Stefansson Vd (1997) Geothermal reinjection experience. *Geothermics* 26(1):99–139
- Stringfellow W, Dobson P (2020) Retrospective on recent doe-funded studies concerning the extraction of rare earth elements & lithium from geothermal brines. Tech. rep., Lawrence Berkeley National Laboratory
- Wang Y, Voskov D, Daniilidis A, et al (2023) Uncertainty quantification in a heterogeneous fluvial sandstone reservoir using gpu-based monte carlo simulation. *Geothermics* 114:102773. <https://doi.org/10.1016/j.geothermics.2023.102773>



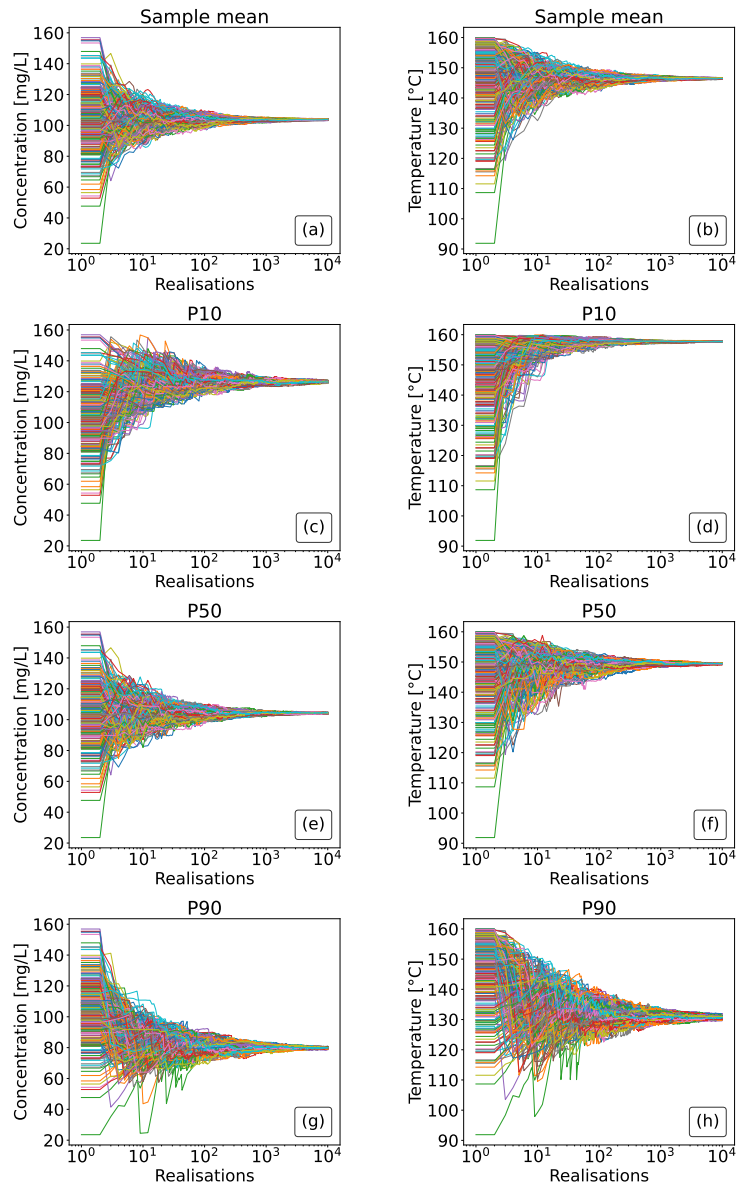


Figure 12: The convergence of the Monte Carlo simulations for the network with 30 fractures. The left column is the concentration, and the right column is the temperature. The rows are the sample mean ((a), (b)), P10 ((c), (d)), P50 ((e), (f)), and P90 ((g), (h)).